Available online at www.sciencedirect.com

ScienceDirect

Procedia CIRP 87 (2020) 176–180

www.elsevier.com/locate/procedia

5th CIRP CSI 2020

Effect of tool coatings on surface grain refinement in orthogonal cutting of AISI 4140 steel

Germán González[a,*], Marcel Plogmeyer[b], Frederik Zanger[a], Saskia Biehl[c], Günter Bräuer[b], Volker Schulze[a]

[a]*wbk Institute of Production Science, Karlsruhe Institute of Technology (KIT), Kaiserstr. 12, 76131 Karlsruhe, Germany*
[b]*TU Braunschweig, Institute for Surface Technology (IOT), Bienroder Weg 54E, 38108 Braunschweig, Germany*
[c]*Fraunhofer Institute for Surface Engineering and Thin Films (IST), Bienroder Weg 54E, 38108 Braunschweig, Germany*

* Corresponding author. Tel.: +49-721-608-42455; fax: +49-721-608-45004. *E-mail address:* german.gonzalez@kit.edu

Abstract

Recrystallization mechanisms leading to the generation of ultrafine grains (UFG) by surface severe plastic deformation (S^2PD) at low temperatures ($< 0.5T_m$ (melting temperature)) have been investigated over the last years. Material removal processes like broaching impose large plastic strains along the shear plane during chip formation, leading in many cases to changes in the workpiece subsurface microstructure. In this work the influence of the cutting material on surface grain recrystallization were studied on broaching of AISI 4140q&t steel. Orthogonal cutting tests were carried out in dry conditions on a broaching machine using tools with different coatings. Uncoated cemented carbide inserts were geometrically prepared using fixed abrasive grinding processes and then coated by physical vapor deposition (PVD) with Al_2O_3 and CrVN thin films. Workpiece subsurface layers were analyzed after machining by Focused Ion Beam (FIB-SEM) and X-ray diffraction (XRD). The presented results show the influence of the cutting material on the final microstructure of the machined workpieces through the determination of the final grain sizes and dislocation densities.

Keywords: machining; grain refinement; coated tools

1. Introduction

Despite the large number of new manufacturing technologies that enter the industrial field, material removal processes still show dominance due to its flexibility and performance. This prevalence over the years has been achieved thanks to the effort of many professionals to satisfy the needs of an industry, in which the functional specifications are increasingly high. Many of the key performance indicators for measuring quality of a machined component in terms of mechanical properties are summarized under the name of Surface Integrity [1]. New strategies to improve the functional performance such as fatigue life, wear resistance and hardness were studied over the last years. In this work, one of those strategies, the generation of ultrafine grains structures (UFG) in the workpiece subsurface during machining [2-4] was studied under new boundary conditions. The influence of coated and uncoated cemented carbide tools on the subsurface microstructure in orthogonal cutting operations was analyzed. The tools were prepared using abrasive grinding methods in order to minimize the influence of other factors like cutting edge microgeometries on the microstructural changes [5]. Physical vapor deposition (PVD) technology was used for thin film coating. Using Focused Ion Beam in combination with Scanning Electron Microscopy (FIB-SEM) and X-ray diffraction (XRD) the changes in the workpiece microstructure were determined. In addition, these microstructural variations were related with the increase in dislocation density produced during the machining process.

10.1016/j.procir.2020.02.113

2. Tool and workpiece set-up

2.1. Cutting tool surface and edge preparation

It is well known that the cutting edge radius has a remarkable influence on the surface finishing and subsurface damage, changing important factors such as temperature distribution or material flow during machining. Cutting tools with negative rake angles and high ratio between cutting edge radius r_β and uncut chip thickness h, known as relative roundness, induce greater changes in the grain microstructure of the machined workpiece [5]. With the purpose of reducing the effect of relative roundness, rake and flank face of cemented carbide inserts with geometry SNGA 190908 were prepared by plunge-face grinding [6]. A Buehler planar grinder was used in combination with diamond grinding discs of different grain diameters. The rotation speed was set to 150 rpm and the grinding pressure to 35 N. Symmetrically rounded cutting edge radius r_β = 5 µm were obtained. To improve the quality of the subsequent coating process, the tool surfaces were also ground and polished obtaining surface roughness values of less than R_z = 0.1 µm. The inserts were characterized by measurement of the edge profile and flank face roughness. A Mahr perthometer was used for measuring the prepared cutting edge profiles. Surface roughness was identified by a confocal light microscope of NanoFocus [7].

2.2. Insert coatings

The cemented carbide tools were coated using Physical Vapor Deposition (PVD) processes. Aluminum oxide (Al_2O_3) thin films were deposited by Radio Frequency (RF) magnetron sputtering from an oxide target on rake and flank face separately using masking to ensure homogeneous deposition at the edges and the faces. Thicknesses of 4.5 µm and 3 µm were achieved respectively. A wear-resistant coating such as chromium vanadium nitride (CrVN) was deposited on inserts already coated with Al_2O_3 by Direct Current (DC) magnetron sputtering with a thickness of 4 µm.

The thermal conductivity k is a key factor for the evaluation of the results of this work and in consequence was determined for each cutting material. For the Al_2O_3 coatings, separate samples were prepared for experimental characterization with an extension of the 3ω-method [8]. A value k = 1.6 $W \cdot m^{-1} \cdot K^{-1}$ was obtained for 4.4 µm thick Al_2O_3 layer at 25°C. At elevated temperatures Al_2O_3, due to its chemical stability, presents slight variations in its thermal conductivity achieving values in the range of k=2-3 $W \cdot m^{-1} \cdot K^{-1}$ for temperatures of 500-600°C [9]. This relatively small thermal conductivity at high temperatures will provide more effective thermal protection to the substrate varying the process temperature distribution. In addition, the fraction of heat carried away by the chip and the depth of heat penetration into the workpiece will increase. Values for cemented carbide ground material (Tungsten carbide WC) are typically around k = 120 $W \cdot m^{-1} \cdot K^{-1}$ [10]. The thermal conductivity values for CrVN were assumed higher than the values of Al_2O_3 according to studies with CrN coatings [11].

2.3. Material and test workpiece

Steel AISI 4140 was austenized at 850 °C, quenched by oil and then tempered at 610°C in a furnace. From 50 mm diameter bars, 80x20x4 mm size workpieces were extracted using wire-EDM with the aim of reducing the microstructural damage [12]. Before machining, the surface of the workpieces were polished to eliminate the oxide-layer generated by the EDM-process. The initial microstructure of the workpieces was measured after polishing and nital etching with the aid of a white light microscope as well as with X-ray diffraction tests for the retained austenite determination.

The microstructure, shown in Figure 1, presents a high content of tempered martensite (~70%) and bainite (~30%) with retained austenite (<1%).

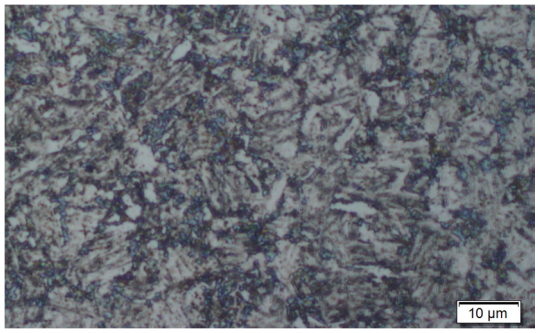

Fig. 1. AISI 4140q&t workpiece microstructure measurement using a light microscope after polishing and etching with nital.

3. Orthogonal cutting tests

Orthogonal cutting tests were carried out without coolant on a Karl Klink vertical broaching machine. As shown in Figure 2, the experimental setup featured a static tool, while a clamped workpiece moves downwards with a set cutting speed, v_c = 150 m/min. Coated and uncoated cemented carbide inserts with cutting edge radius r_β = 5 µm were used. Orthogonal cutting rake, wedge and clearance angles, were set to ɣ = -7°, β = 90° and α = 7°. Cutting path length, width and thickness of the uncut chip thickness were L = 80 mm, b = 4 mm and h = 0.2 mm, respectively.

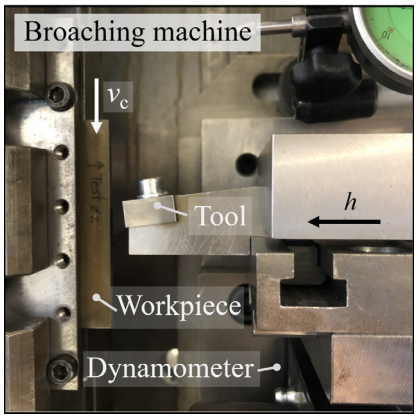

Fig. 2. Set-up of the orthogonal cutting experiments.

Cutting and thrust forces F_c and F_t were measured using a plate dynamometer. Each cutting test was carried out four times using a new workpiece and cutting tool. Process parameters as well as tool coatings are listed in Table 1.

Table 1. Parameters of orthogonal cutting experiments.

Number of test	Tool coating		v_c	h	r_β
	Material	Thickness [µm]	[m/min]	[mm]	[µm]
1-4	-	-	150	0.2	0.45
5-8	Al_2O_3	4.5	150	0.2	0.50
9-12	Al_2O_3 + CrVN	4.5 + 4.0	150	0.2	0.55

The measured cutting forces, shown in Figure 3, present slightly variations due to the coefficient of friction of the different cutting materials.

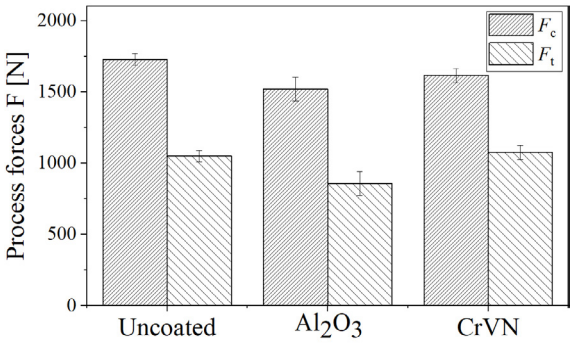

Fig. 3. Cutting force F_c, and thrust force F_t, during orthogonal tests using different coatings.

4. Microstructure gradient analysis

The quantitative microstructure of the workpiece was analyzed using a Focused Ion Beam (FIB) system combined with Scanning Electron Microscopy (SEM). The micro-perforations were performed in the longitudinal direction of the workpieces according to Figure 4. The combination of an ion-optical column, which generates a focused 30 keV Ga^+ ion beam, with a scanning electron microscope allows to "mill" nanostructures and to identify the crystallographic micro-structure and chemical composition respectively.

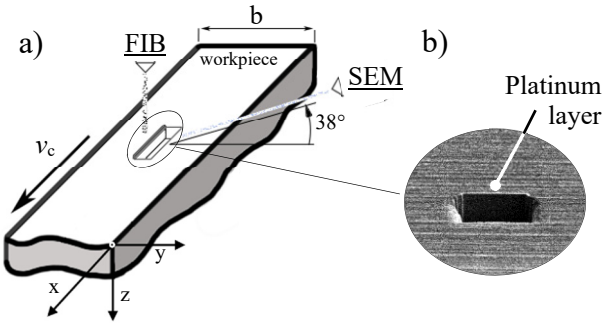

Fig. 4. a) Schematic representation of the measuring area of the workpiece using FIB+SEM technique, b) SEM image of the perforated area.

A thin layer of platinum was deposited on the surface of the workpiece close to the perforated area, to reduce the effect of surface roughness on the measurements. The microstructure gradients of the workpiece cross-sections, shown in Figure 5, present three different sections.

- The first section (I) results from the combination of severe plastic deformations (SPD), grain phase transformations and high thermal gradients. Consequently, the grains were recrystallized and finally refined giving rise to an ultrafine grain (UFG) structure with grain sizes below 100 nm.
- Below this layer, a microcrystalline sheared layer with a grain size less than 1 µm conforms the second section (II).
- A plastic deformed transition area to bulk material corresponds to the third section (III) [13].

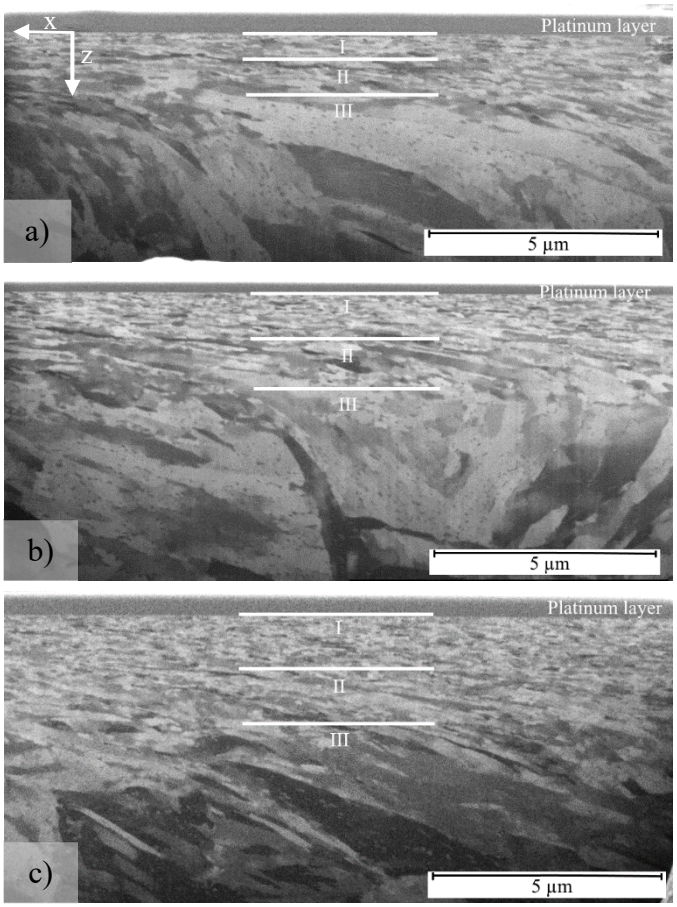

Fig. 5. FIB image of cross-sections graded microstructures obtained after broaching using: a) uncoated, b) Al_2O_3 coated and c) CrVN + Al_2O_3 coated tools.

Due to the restrictions of the measuring device, it was not possible to perforate the surface deep enough to visualize the bulk material. The measurements shown in Figure 5 were processed using a pixel count algorithm and the thickness of the three sections according to the grain size were determined and plotted in Figure 6. Thicker recrystallized grain layers were generated by the coated tools as a result of higher temperature rise in the tertiary zone.

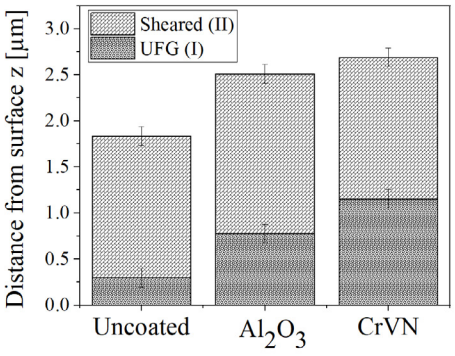

Fig. 6. Thickness of the UFG (I) and sheared (II) layers of the machined workpieces measured using FIB-SEM.

The use of different cutting materials translates into a different distribution of the process temperature in the tool-workpiece contact area. Cutting tools coated with layers of lower thermal conductivity that act as a thermal barrier produce higher temperature flow to the chip and to the workpiece during the cutting process inducing higher thermal strains and thermally driven phase transformations.

5. Crystalline structures analysis

X-ray diffraction (XRD) provides information about crystal structure and defect structure. For example, lattice strain mainly resulting from dislocations stored in the subsurface regions were obtained by determining broadening of ferrite Bragg peaks. Separation from other sources of broadening, e.g. broadening by nanometer-sized coherent domains can be achieved by using the Williamson-Hall approach (WH) [14]:

$$\delta \frac{\cos\theta}{\lambda} = \frac{k_s}{d} + 2\varepsilon \frac{\sin\theta}{\lambda} \tag{5.1}$$

where δ is the full width at half maximum (FWHM) of the Bragg peaks (peak position θ) obtained in a Bragg-Brentano XRD set up, d is the average domain size, λ is the X-ray wave length, ε is the lattice strain and k_s is approx. 0.9

A more convenient representation can be obtained by introducing the scattering vector S:

$$S = 2\frac{\sin\theta}{\lambda} \tag{5.2}$$

and by expressing the FWHM as a function of its respective differentiation ΔS:

$$\Delta S = \frac{k_s}{d} + \varepsilon\, S \tag{5.3}$$

XRD measurements were performed using a D2 phaser device by Bruker operating with Cu Kα radiation. The Cu tube was used at 30 kV and 10 mA.

The diffraction pattern was detected using a LynxEye line detector at a step size of 0.01° in 2θ at an accumulated time of 384 s per step. Flourescence radiation by Fe was discriminated by proper LynxEye settings. FWHM were determined by single-peak fitting and were corrected by $K\alpha_1$- $K\alpha_2$ splitting. Figure 7 displays the WH plot for the ferrite phase. A significant broadening of the Bragg peaks is observed due to the local, plastic deformation as can be seen from comparison with the bare substrate, which was prepared by standard metallographic procedures and subsequent etching to avoid surface damage prior to XRD.

However, peak width does not linearly scale with scattering vector as frequently observed in metals and alloys and in contrast to the simple WH approach.

An anisotropic progression of the peak widths different sets of lattice planes is evident. In a first attempt, direction-depending elastic moduli were considered as a potential factor.

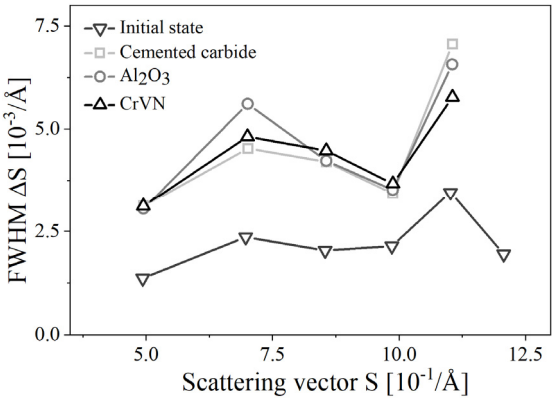

Fig. 7. XRD measurement using different coatings

From Eq. 5.3 it is know that the relation between k_s and d is the domain size and is measured as the size of coherently scattering areas (when d << 1 µm) and the slope is a measure for the dislocation density.

When the grain size is less than 1 µm and combining Eq. 5.3 with the magnitude of the burgers vector b, the Williamson and Smallman equation [15] is obtained and the dislocation density in the subsurface can be determined by:

$$\rho = \frac{\varepsilon^2}{b^2} \tag{5.4}$$

The dislocation density values for the machined workpieces are in the range of $\rho = (2 - 4)\cdot 10^{15}$ m^{-2}. As reference, the dislocation density of a workpiece before machining was also determined $\rho = (0.8 - 1)\cdot 10^{15}$ m^{-2}.

These results must be treated with a grain of salt as there are many factors other than dislocation density, coherent domain size and elastic anisotropy that affect the peak broadening significantly, e.g. other defects that occur during plastic deformation, such as stacking faults, strain-induced martensite, etc., which also contribute to the peak width.

In addition, the contrast factors for dislocations depend on the respective set of lattice planes.

Furthermore, severe plastic deformation leads to distinct dislocations structures and networks with high and low dislocation density.

5.1. Grain size and dislocation density

The relation between the grain size gradient structure and the lattice distortion helps to predict the grain recrystallization produced by the extreme conditions of machining processes. Through Eq. (5.5) the domain size d and the total dislocation density ρ can be related using a proportional constant, K [16].

$$d = \frac{K}{\sqrt{\rho}} \tag{5.5}$$

The value of K must be studied experimentally in detail. As explained previously in this chapter, it is very difficult to determine the dislocation density in the results due to the numerous influential factors. An increment in the dislocation density does not always mean a decrease in domain size. For instance, a high thermal gradient can recrystallize the grains into bigger structures. In addition, the time during which a thermal load is applied is an important factor to consider to determine K and to identify the recrystallization mechanisms, e.g. static and dynamic (DRX).

6. Outlook and future directions

A comparative experimental study of the effect of different tool materials on the subsurface deformed layer on broaching of AISI 4140q&t was carried out. Through the tool preparation and a proper process parameter selection, factors such as relative roundness and rake surface quality did not influence the results significantly. For the analysis, X-ray diffraction (XRD) and Focused Ion Beam (FIB) combined with Scanning Electron Microscopy (SEM) were used. It has been demonstrated how tools coated with Al_2O_3 and CrVN generate greater changes in the microstructure of the workpiece subsurface than uncoated cemented carbide tools. These changes were attributed to the different values of thermal conductivity of the cutting materials.

- Machined workpieces using coated tools presented an ultrafine grained (UFG) layer up to twice as thick than the machined workpieces using uncoated tools.
- The dislocation density of the workpieces increased up to 50 times after machining.
- The variation in the dislocation density produced by the different cutting materials did not present a clear tendency.

Using deterministic methods like FEM analysis and considering the grain recrystallization phenomena based on geometrical and statistical dislocation density in the constitutive material model, the stochastic character of the machining process can be better described with no need to reach the atomic level. This leads to an increase in accuracy of the predictions and a reduction of calculation time. In order to model the recrystallization mechanisms and the final grain structures in a proper way and according with this approach, a better understanding of the relation between microstructural changes during severe plastic deformations and the increase in dislocation density is needed. For future work, changes in the dislocation density fluctuations during plastic deformation on steel with different heat treatments will be systematically studied using XRD with the aim of better peak broadening adjustment and characterization.

Acknowledgements

The scientific work has been supported by the DFG within the research priority program SPP 2086. The authors thank the DFG (SCHU 1010/63-1) and (BR 2178/47-1) for this funding and intensive technical support. The present authors appreciate support of Dr.-Ing. A. Kauffmann and Dr.-Ing. S. Seils of IAM-WK institute (Karlsruhe Institute of Technology) for the XRD measurements and the encouraging discussions.

References

[1] Arrazola P.J, Özel T, Umbrello D, Davies M, Jawahir I.S. Recent advances in modelling of metal machining processes. CIRP Annals-Manufacturing Technology 2013; 62:695-718.
[2] Jawahir I.S, Brinksmeier E, M'Saoubi R, Aspinwall D, Outeiro J, Meyer D, Umbrello D, Jayal AD. Surface integrity in material removal processes: recent advances. CIRP Annals-Manufacturing Tech. 2011; 60:603-626.
[3] D, Umbrello. Influence of material microstructure changes on surface integrity in hard machining of AISI 52100 steel. Int J Adv Manuf Technol 2011; 54: 887-898.
[4] Outeiro J.C, Kandibanda R, Pina J.C, Dillon O.W, Jawahir I.S. Size-effects and surface integrity in machining and their influence on product sustainability. Int. J. Sustainable Manufacturing 2010; 2: 112-126.
[5] Ambrosy F, Zanger F, Schulze V. FEM-simulation of machining induced nanocrystalline surface layers in steel surfaces prepared for tribological applications. CIRP Annals- Manufacturing Technology 2015; 64:69-72.
[6] Denkena B, Köhler J, Breidenstein B, Abrão A.M, Ventura C.E.H. Influence of the cutting edge preparation method on characteristics and performance of PVD coated carbide inserts in hard turning. Surface and Coatings Technology 2014; 254: 447-454.
[7] Holsten S, Tikal F. Schneidkantenpräparation: Ziele, Verfahren und Messmethoden. Kassel University Press, Kassel 2009; 12-33.
[8] Cahill D. G., Katiyar M., Abelson J. R. Thermal conductivity of a-Si:H thin films. Physical review 1994; 50: 6077.
[9] Lee S. M, Cahill D. G, Allen T. H. Thermal conductivity of sputtered oxide films. Physical Review 1995; 52: 253-257.
[10] Schultrich B. and Poeßnecker W**.** Thermal conductivity of cemented carbides. J Therm Anal Calorim 1988; 33: 305-310.
[11] Tlili B, Nouveau C, Walock M.J, Nasri M, Ghrib T. Effect of layer thicknesson thermal properties of multilayer thin films produced by PVD. Vacuum, Elsevier 2012; 86: 1048-1056.
[12] Bleys P, Kruth J-P, Lauwers B, Schacht B, Balasubramanian V, Froyen L, Van Humbeeck J. Surface and Sub-Surface Quality of Steel after EDM. Advanced Engineering Materials 2006; 8: 15-25.
[13] Zanger F, Gerstenmeyer M, Hartmut W. Identification of an optimal cutting edge microgeometry for Complementary Machining. CIRP Annals-Manufacturing Technology 2017; 66: 81-84.
[14] Williamson G.K. and Hall W.H. X-ray line broadening from filed aluminium and wolfram. Acta Metallurgica I 1953; 1: 22-31.
[15] Williamson G.K. and Smallman. Dislocation densities in some annealed and cold-worked metals from measurements on the X-ray debye-scherrer spectrum. The Philosophical Magazine: A Journal of Theoretical Experimental and Applied Physics 1956; 1: 34-46.
[16] Estrin Y, Tóth L.S, Molinari A, Bréchet Y. Dislocation-based model for all hardening stages in large strain deformation. Acta Materialia 1998; 15:5509-55.